

# Stabilizing the Interface between Sodium Metal Anode and Sulfide-Based Solid-State Electrolyte with an Electron-Blocking Interlayer

Pu Hu,<sup>†</sup> Ye Zhang,<sup>†</sup> Xiaowei Chi,<sup>†</sup> Karun Kumar Rao,<sup>‡,||</sup> Fang Hao,<sup>†,||</sup> Hui Dong,<sup>†,||</sup> Fangmin Guo,<sup>§</sup> Yang Ren,<sup>§</sup> Lars C. Grabow,<sup>‡,||,||</sup> and Yan Yao<sup>\*,†,‡,||,||</sup>

<sup>†</sup>Department of Electrical and Computer Engineering and Materials Science and Engineering Program, University of Houston, Houston, Texas 77204, United States

<sup>‡</sup>Department of Chemical and Biomolecular Engineering, University of Houston, Houston, Texas 77204, United States

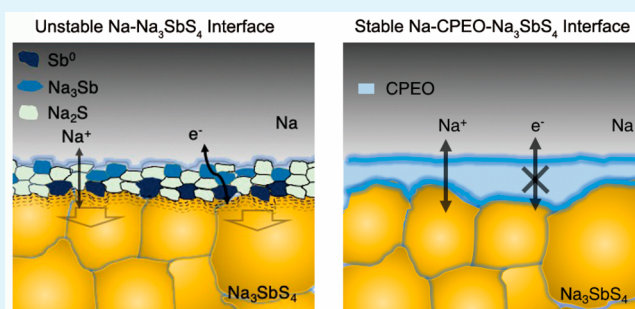
<sup>§</sup>X-ray Science Division, Argonne National Laboratory, Argonne, Illinois 60439, United States

<sup>||</sup>Texas Center for Superconductivity at the University of Houston, Houston, Texas 77204 United States

## Supporting Information

**ABSTRACT:** Sulfide-based Na-ion conductors are promising electrolytes for all-solid-state sodium batteries (ASSSBs) because of high ionic conductivity and favorable formability. However, no effective strategy has been reported for long-duration Na cycling with sulfide-based electrolytes because of interfacial challenges. Here we demonstrate that a cellulose-poly(ethylene oxide) (CPEO) interlayer can stabilize the interface between sulfide electrolyte ( $\text{Na}_3\text{SbS}_4$ ) and Na by shutting off the electron pathway of the electrolyte decomposition reaction. As a result, we achieved stable Na plating/stripping for 800 cycles at  $0.1 \text{ mA cm}^{-2}$  in all-solid-state devices at  $60^\circ\text{C}$ .

**KEYWORDS:** Na metal anode, sulfide-based solid electrolyte, polymer composite interlayer,  $\text{Na}_3\text{SbS}_4$ , interfacial stability



Sodium metal is an attractive anode for next-generation energy storage devices owing to its high specific capacity, low cost and high abundance in nature.<sup>1,2</sup> However, Na metal anode has been shown problematic because of uncontrolled dendrite growth and side reactions with liquid electrolytes.<sup>1,3</sup> All-solid-state sodium batteries (ASSSBs) represent a promising solution to prevent Na dendrite growth and eliminate safety concerns posed by flammable organic electrolytes.<sup>2</sup> Oxide-based Na-ion electrolytes such as  $\beta$ -alumina and NASICON-type electrolytes exhibit ionic conductivities higher than  $1 \text{ mS cm}^{-1}$  but require high-temperature sintering.<sup>4</sup> In contrast, sulfide-based solid electrolytes, such as cubic phase  $\text{Na}_3\text{PS}_4$ ,<sup>5</sup> have better formability, lower grain boundary resistance, and comparable ionic conductivity, making it possible to build a bulk-type ASSSBs via cold-pressing method.<sup>6</sup>

Despite the great progress in developing new sulfide-based electrolytes with high ionic conductivity, high-performance ASSSBs remain elusive mainly because of the challenges at the interfaces.<sup>7</sup> Ab initio calculations revealed that sulfide-based electrolytes have a narrow electrochemical window.<sup>8,9</sup> Consequently, electrolytes decompose at the anode interface and properties of the decomposed products largely control the overall cell performance. For example, lithium solid-state electrolytes such as  $\text{Li}_7\text{P}_3\text{S}_{11}$  forms stable solid electrolyte interphases (SEIs) because their decomposition products are

either insulating (e.g.,  $\text{Li}_2\text{S}$ ) or increase the kinetic barriers to decomposition (e.g.,  $\text{Li}_3\text{P}$ ).<sup>10</sup> For sodium electrolytes, the decomposition products (e.g.,  $\text{Na}_3\text{P}$ ) tend to have narrower bandgaps and are more electronically conducting than their lithium analogues.<sup>11,12</sup> The formed mixed-ion electron-conducting interphase promotes continuous electrolyte decomposition and therefore deteriorates battery performance.<sup>12</sup>  $\text{Na}_2\text{Sn}$  alloy anode has been used to alleviate electrolyte decomposition due to lower reactivity than that of Na.<sup>11,13</sup> Table S1 summarizes the cycling performance of Na metal symmetric cells with various sulfide-based solid-state electrolytes.<sup>11,14,15</sup> Although higher ionic conductivity of electrolytes could be achieved with anion substitution or doping,<sup>11,15</sup> their poor stability against Na metal leads to growth in areal specific resistance (ASR) as the cycle number increases. As a result, there is no report of long-term stable cycling of Na metal using sulfide-based solid-state electrolytes, therefore greatly limiting the development of ASSSBs.

In this work, we improve the interfacial stability between sulfide-based solid electrolytes and Na metal by introducing an electron blocking interlayer.  $\text{Na}_3\text{SbS}_4$ , a sulfide-based Na-ion conductor with the highest Na-ion conductivity reported to

Received: November 13, 2018

Accepted: February 26, 2019

Published: February 26, 2019

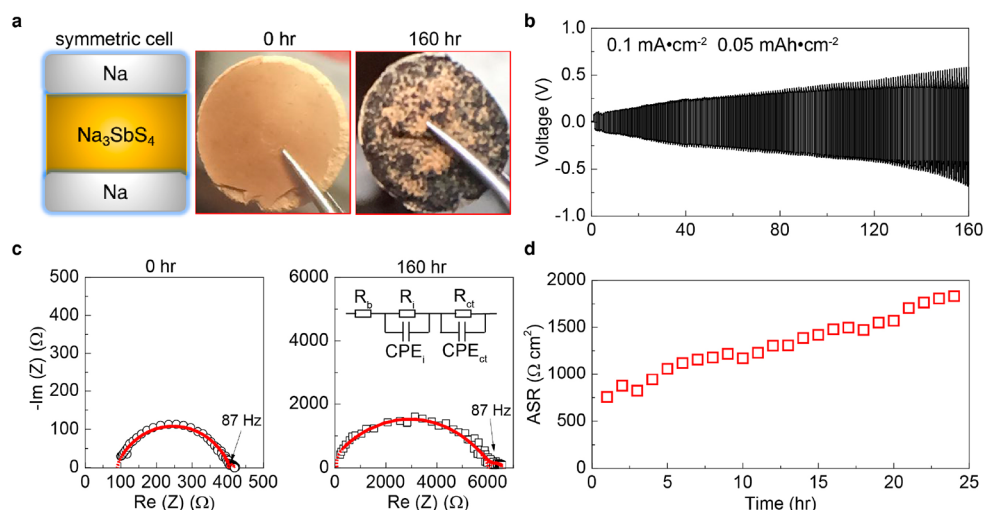


**Figure 1.** Characterization of Na–Na<sub>3</sub>SbS<sub>4</sub> interface instability in a symmetric Na cell. (a) Schematic of the Na/Na<sub>3</sub>SbS<sub>4</sub>/Na symmetric cell and photos of Na<sub>3</sub>SbS<sub>4</sub> electrolyte pellet before and after 160 h of operation. (b) Galvanostatic voltage profile of the cell cycled at a current density of 0.1 mA cm<sup>-2</sup> for 0.5 h Na deposition and 0.5 h Na stripping during each cycle at 60 °C after 1 h rest at the beginning of cycling. (c) Nyquist plots of electrochemical impedance spectroscopy at 60 °C at 0 and 160 h, showing the increasing impedance with the time of cycling. Equivalent circuit (inset) is employed to fit the data with the fitting parameters shown in Table S2. (d) Evolution of total area specific resistance (ASR) during the first 25 h.

date,<sup>16–18</sup> was chosen as a model electrolyte. Through a combination of synchrotron-based diffraction and absorption measurements and computational modeling, we have identified Na<sub>2</sub>S and Sb as the main decomposition products of the electrolyte during the electrochemical process. The mixed ion-electron-conducting interphase leads to continuous decomposition of electrolyte and was reflected in an ever-increasing ASR vs time. To improve the interfacial stability, we have demonstrated an effective approach using an electronically insulating cellulose–poly(ethylene oxide) (CPEO) interlayer between Na metal and Na<sub>3</sub>SbS<sub>4</sub> to shut off the electron pathway for the decomposition reaction. A Na–Na symmetric cell using CPEO/Na<sub>3</sub>SbS<sub>4</sub>/CPEO trilayer electrolyte shows stable Na plating/stripping for 800 cycles (800 h) at a current density of 0.1 mA cm<sup>-2</sup>.

We synthesized tetragonal Na<sub>3</sub>SbS<sub>4</sub> powder by dehydrating Na<sub>3</sub>SbS<sub>4</sub>·9H<sub>2</sub>O following the work of Liang et al.<sup>17</sup> The advantage of this dehydration method is that it allows for low-temperature heat treatment from a commercially available product. However, the Na<sub>3</sub>SbS<sub>4</sub>·9H<sub>2</sub>O compound may contain minor NaSb(OH)<sub>6</sub> impurity. Figure S1 compares the powder X-ray diffraction patterns before and after removing the crystalline water of Na<sub>3</sub>SbS<sub>4</sub>·9H<sub>2</sub>O. The Raman spectrum of the Na<sub>3</sub>SbS<sub>4</sub> powder shows three distinct peaks which belong to the SbS<sub>4</sub><sup>3-</sup> unit (Figure S2a). After cold-pressing the synthesized powder, we measured Na-ion conductivity of the Na<sub>3</sub>SbS<sub>4</sub> pellet to be 1.0 mS cm<sup>-1</sup> at room temperature with an activation energy of 0.24 eV (Figure S2b), which agrees with the literature value of 0.22 eV.<sup>17</sup>

The intrinsic electrochemical stability between Na<sub>3</sub>SbS<sub>4</sub> and Na metal was studied using a Na–Na symmetric cell (Figure 1a). After cell fabrication and resting at 60 °C for 1 h, the symmetric cell was cycled at a current density of 0.1 mA cm<sup>-2</sup> for 0.5 h of Na plating and 0.5 h of stripping for a total of 160 cycles. Figure 1b shows the overpotential of the cell increased monotonically against cycling time. During the initial 25 h, the calculated ASR increased from 750 to 1,860 Ω cm<sup>2</sup> (Figure 1d). We compared the electrochemical impedance spectroscopy (EIS) spectra of the symmetric cell before and after cycling (Figure 1c).

The equivalent circuit is shown in the inset and the fitting parameters are in Table S2. Bulk resistance ( $R_b$ ) had almost no change before and after cycling (from 87.2 to 90.9 Ω). However, the interfacial resistance between the Na<sub>3</sub>SbS<sub>4</sub> and Na ( $R_i$ ) increased significantly from 318.2 to 6,475.0 Ω and charge-transfer resistance ( $R_{ct}$ ) increased from 13.6 to 464.3 Ω. The cell was disassembled after 160 h inside a glovebox and the electrolyte surface was found to be roughened with black areas clearly visible (Figure 1a), indicating an unstable interface between Na and Na<sub>3</sub>SbS<sub>4</sub>. The black areas shown in the figure are expected to be micron-sized Na formed during the plating process (Figure S3).

Meng et al. recently studied the chemical stability of Na<sub>3</sub>SbS<sub>4</sub> against Na metal and identified Na<sub>3</sub>Sb and Na<sub>2</sub>S as the major Na-solid electrolyte interphase components.<sup>15</sup> Our hypothesis is that similar reaction takes place during the electrochemical cycling process. To confirm the hypothesis, the electrolyte/metal interface was analyzed using synchrotron-based X-ray diffraction (XRD), X-ray absorption near edge structure (XANES), and X-ray photoelectron spectroscopy (XPS). The pristine Na<sub>3</sub>SbS<sub>4</sub> sample was also measured for comparison. Figure 2a shows that the XRD pattern of the pristine sample can be indexed as tetragonal phase Na<sub>3</sub>SbS<sub>4</sub> with minor NaSb(OH)<sub>6</sub> impurities formed during the synthetic process. The hydroxide has a negligible effect on the overall conductivity and electrolyte stability as its amount is only 3 mol %. After cycling with Na metal for 160 h, two new peaks appeared at 1.78 and 2.91°, which are indexed as Na<sub>2</sub>S (111) and Na<sub>2</sub>S (220) plane. For the XPS analysis, S 2p and Sb 3d regions are shown in Figure 2b. For pristine Na<sub>3</sub>SbS<sub>4</sub> sample, the S 2p spectrum can be fitted with two spin-orbit doublets, which correspond to the Sb=S and Sb–S–Na bonds. The cycled sample showed a decrease in intensity of the Sb–S–Na bond, whereas a relatively weak doublet appeared at a lower binding energy of 159.3 eV (red), corresponding to the Na–S bond. For the Sb 3d spectra, pristine Na<sub>3</sub>SbS<sub>4</sub> sample shows a single doublet of Sb–S bond

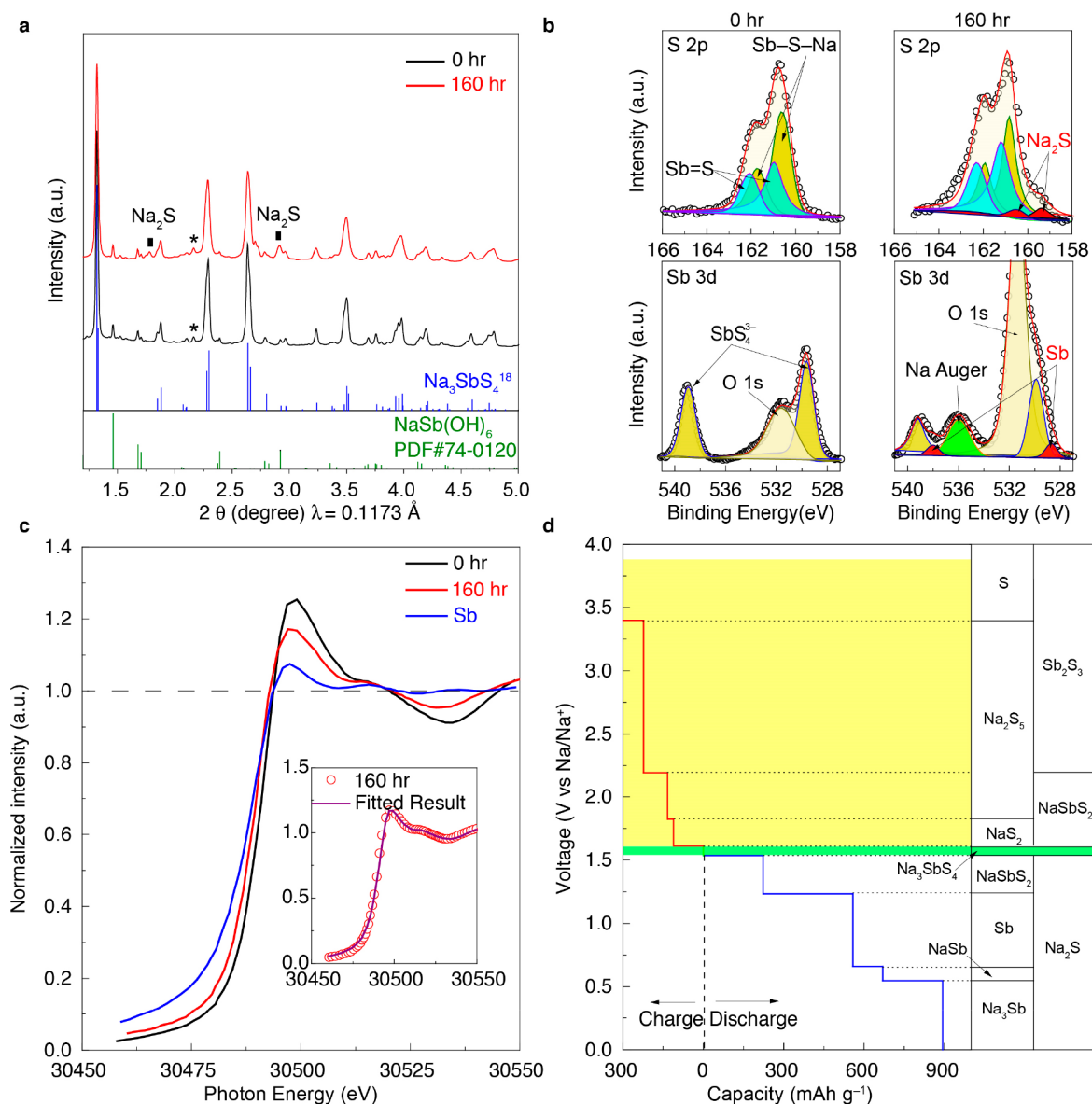


**Figure 2.** Investigate the decomposition products at  $\text{Na}-\text{Na}_3\text{SbS}_4$  interface via theoretical and experimental approaches. (a) X-ray diffraction patterns of  $\text{Na}_3\text{SbS}_4$  at 0 h (black) and 160 h (red) of cycling. The standard  $\text{Na}_3\text{SbS}_4$  patterns from ref 18 and  $\text{NaSb(OH)}_6$  patterns are used for peak indexation. The peak marked with asterisks at  $2.15^\circ$  is an unknown impurity. Peaks marked with black squares correspond to  $\text{Na}_2\text{S}$ . At  $2.9^\circ$ , the  $\text{Na}_3\text{SbS}_4$  and  $\text{Na}_2\text{S}$  peaks are close but the presence of  $\text{Na}_2\text{S}$  would result in an additional peak at  $1.75^\circ$  which was not observed at 0 h. (b) High-resolution XPS spectra of S 2p and Sb 3d. The O 1s peak around 532 eV represents the oxygen-containing impurities generated during the material synthesis. The peak at 536 eV represents the Auger peak of Na metal. The appearance of  $\text{Na}_2\text{S}$  and Sb peaks are clearly visible at 160 h, indicating the decomposition of  $\text{Na}_3\text{SbS}_4$ . (c) The Sb K-edge XANES spectra of metallic Sb reference sample,  $\text{Na}_3\text{SbS}_4$  samples at 0 and 160 h. The inset shows the curve fitting using Sb and  $\text{Na}_3\text{SbS}_4$  with weight fractions of 45.6 and 54.4%, respectively. (d) Calculated equilibrium voltage profile and phase equilibria for sodiation and desodiation reactions of  $\text{Na}_3\text{SbS}_4$ .  $\text{Na}_2\text{S}$  and  $\text{Na}_3\text{Sb}$  are the predicted decomposition products when in contact with metallic Na at 0 V. The corresponding phase diagram of  $\text{Na}-\text{Sb}-\text{S}$  is shown in Figure S4 and the stable voltage window for each phase equilibrium is shown in Table S3.

in the  $\text{SbS}_4^{3-}$  tetrahedron. After cycling, another doublet appears, corresponding to metallic Sb.<sup>15</sup> The weak XPS signal of Sb was a result of the low atomic ratio of Sb in the compound. Therefore, we measured XANES to provide additional evidence to support the existence of Sb. The XANES results were collected at the Beamline 20 BM at the Advanced Photon Source. Figure 2c shows the XANES Sb K-edge spectra for three samples: pristine  $\text{Na}_3\text{SbS}_4$  powder (black), the sample after 160 cycles (red), and metallic Sb as a reference (blue). There is a ca. 1.6 eV shift in the onset absorption edge between Sb and  $\text{Na}_3\text{SbS}_4$  spectra, attributing

to the oxidation state difference.<sup>19</sup> The onset absorption peak of cycled sample lies in between the black and blue curves, implying it is a mixture of Sb and  $\text{Na}_3\text{SbS}_4$ . On the basis of the linear combination fitting of the Sb K-edge spectra, we find the weight fractions of Sb and  $\text{Na}_3\text{SbS}_4$  as 45.6 and 54.4% (Figure 2c inset and Table S4).

Calculations of the thermodynamic phase equilibria for sodiation and desodiation reactions of  $\text{Na}_3\text{SbS}_4$  further support the observed composition change of the interfacial products during electrochemical cycling. We use a modified chemical potential method proposed by Ong et al.<sup>20</sup> in the phase

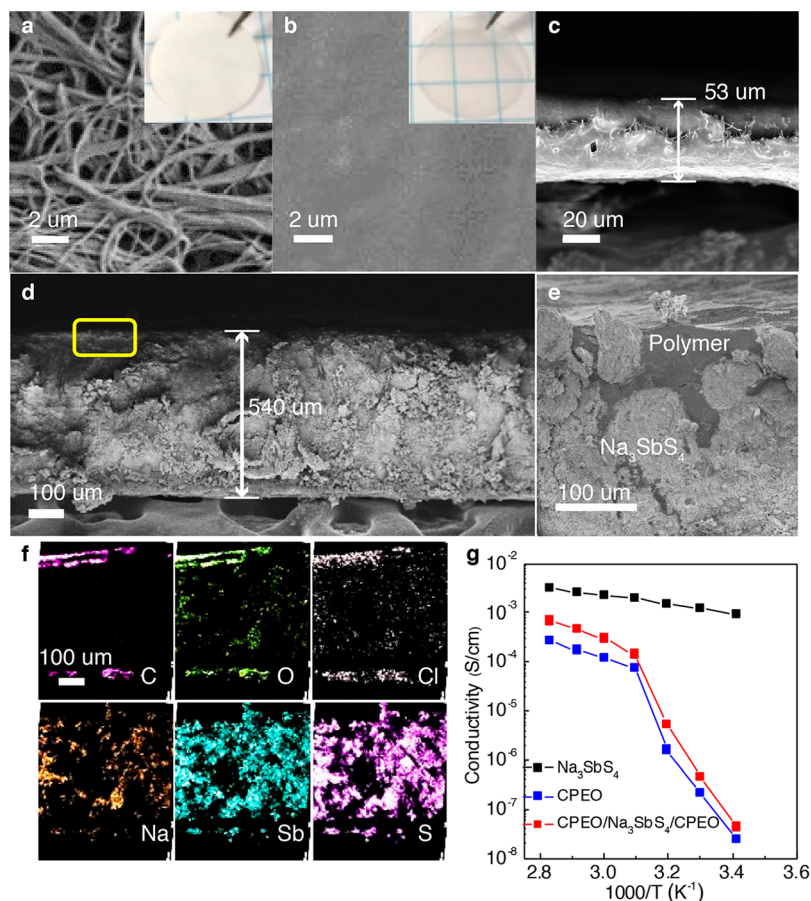


**Figure 3.** Characterizations of CPEO/Na<sub>3</sub>SbS<sub>4</sub>/CPEO composite solid electrolyte. (a) SEM image of a cellulose template. Optical images are shown in the insets. (b, c) Top view and side view of CPEO electrolyte. (d, e) Cross-sectional SEM image of CPEO/Na<sub>3</sub>SbS<sub>4</sub>/CPEO electrolyte with a thickness of 540 μm. Zoom-in SEM image is the highlighted area in a yellow rectangular. (f) Energy-dispersive X-ray spectroscopy (EDS) mapping of cross-sectional CPEO/Na<sub>3</sub>SbS<sub>4</sub>/CPEO trilayer electrolyte. (g) Arrhenius plots of Na-ion conductivity versus reciprocal temperature for Na<sub>3</sub>SbS<sub>4</sub> (black), CPEO (blue), and CPEO/Na<sub>3</sub>SbS<sub>4</sub>/CPEO trilayer electrolyte (red).

diagram modules of Pymatgen<sup>21,22</sup> to calculate which compounds in the Na–Sb–S system are thermodynamically favored at the Na–Na<sub>3</sub>SbS<sub>4</sub> interface at various voltages. The Na<sub>3</sub>SbS<sub>4</sub> electrolyte is modeled in contact with a reservoir of sodium held at a constant potential  $\mu_{\text{Na}}$  which is related to the voltage ( $V$ ) by

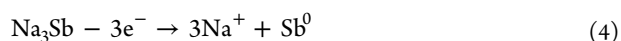
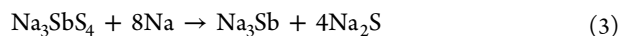
$$V = \frac{\mu_{\text{Na}} - \mu_{\text{Na}}^0}{e} \quad (1)$$

where  $\mu_{\text{Na}}^0$  is a reference chemical potential of sodium, and  $e$  is the elementary charge. The phase stability was assessed at various chemical potentials  $\mu_{\text{Na}}$  with respect to the grand potential

$$\Omega(c, \mu_{\text{Na}}) = E(c) - \mu_{\text{Na}} N(c) \quad (2)$$

where  $E(c)$  is the ground state energy, and  $N(c)$  is the number of sodium atoms in phase  $c$ . Among all compounds in the Na–Sb–S system, stable phases were identified to have the lowest energies at a given voltage in the corresponding grand potential diagram.<sup>21</sup> Mixing and entropic effects are neglected. All phase energy data was obtained from the Materials Project Database.<sup>22</sup> Figure 2d shows the stability plot of Na<sub>3</sub>SbS<sub>4</sub> as a function of Na voltage at 0 K. It predicts that Na<sub>3</sub>SbS<sub>4</sub> is thermodynamically stable only within a narrow potential range of 1.5–1.6 V vs Na/Na<sup>+</sup>. When Na<sub>3</sub>SbS<sub>4</sub> is in direct contact

with Na metal, Na<sub>3</sub>Sb and Na<sub>2</sub>S are predicted as stable phases, which agrees with the results from Meng et al.<sup>15</sup> During the electrochemical process of the symmetric cell test, Na extraction from the formed Na<sub>3</sub>Sb could happen, resulting in the formation of Sb as detected by XPS and XANES. The decomposition reactions of Na<sub>3</sub>SbS<sub>4</sub> are summarized as follows



We have now shown that Na<sub>3</sub>SbS<sub>4</sub> decomposition into Na<sub>2</sub>S and Sb is favorable during electrochemical cycling with a Na metal anode. The mixed ion-electron-conducting interfacial products (Na<sub>2</sub>S and Sb) promote continuous decomposition of Na<sub>3</sub>SbS<sub>4</sub> and are identified as the root cause of unstable interface which led to escalating ASR vs cycle time. To suppress the identified decomposition reaction, an ionic conducting and electronically insulating CPEO film was designed and fabricated as an interlayer to stabilize Na metal/electrolyte interface by ting off the electronic pathway.

The CPEO film was prepared by drop-casting the PEO–NaClO<sub>4</sub> solution onto a cellulose membrane (~20 μm thick), which serves as a scaffold for the film (Figure 3a). After infiltrating PEO–NaClO<sub>4</sub> (EO: Na = 20:1), the composite layer shows a smooth and uniform morphology (Figure 3b). The cross-sectional SEM image reveals the thickness of the

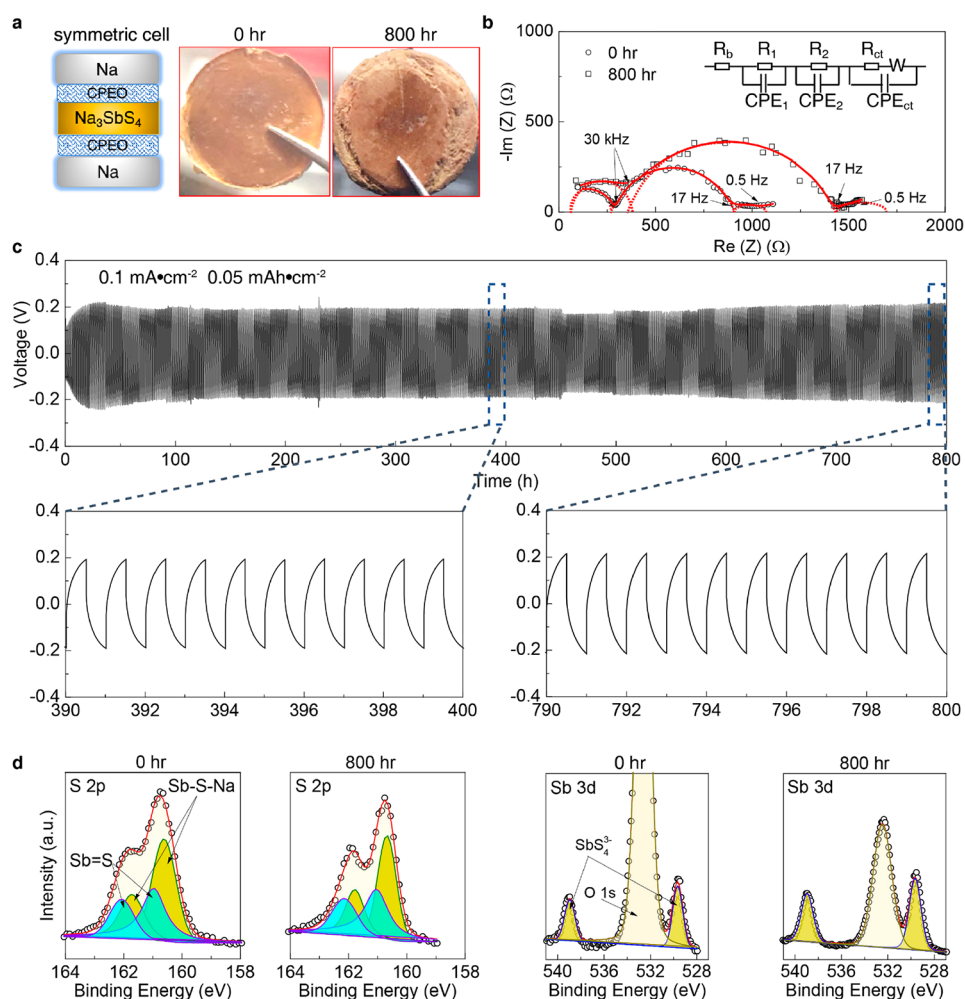


**Figure 4.** Stabilizing metallic Na cycling via CPEO/Na<sub>3</sub>SbS<sub>4</sub>/CPEO trilayer electrolyte. (a) Schematic of the Na/CPEO/Na<sub>3</sub>SbS<sub>4</sub>/CPEO/Na symmetric cell and optical images of the trilayer electrolyte pellet before (0 h) and after cycling (800 h). (b) Nyquist plots of electrochemical impedance spectroscopy at 60 °C at 0 and 800 h, showing slower impedance increase compared to the case without the polymer layer. Equivalent circuit (inset) is employed to fit the data with the fitting parameters shown in Table S2. (c) Galvanostatic voltage profile of the cell cycled at a current density of 0.1 mA cm<sup>-2</sup> for 0.5 h Na plating/stripping during each cycle at 60 °C. Voltage profiles highlighted during the 390–400 h and 790–800 h shows nonsquare profile due to the low transference number of CPEO layer. (d) High-resolution XPS spectra for S 2p and Sb 3d for the Na<sub>3</sub>SbS<sub>4</sub> pellet surface characterization after the CPEO layer is removed. No Na<sub>2</sub>S and Sb peaks are observed at 800 h, indicating the suppressed decomposition of Na<sub>3</sub>SbS<sub>4</sub>. O 1s peak originates from the residual NaClO<sub>4</sub> salt on the surface of Na<sub>3</sub>SbS<sub>4</sub> pellet.

polymer composite around 53  $\mu\text{m}$  (Figure 3c). The thinnest CPEO film we could cast using this method was around 50  $\mu\text{m}$ . Other film preparation methods, such as blade-coating and tape-casting, may effectively reduce the film thickness. The trilayer electrolyte was prepared by sandwiching CPEO films on both sides of Na<sub>3</sub>SbS<sub>4</sub> with a thickness of 540  $\mu\text{m}$  (Figure 3d). The zoomed-in SEM image clearly visualizes the intimate contact between Na<sub>3</sub>SbS<sub>4</sub> and CPEO (Figure 3e) as the polymer electrolyte filled into the surface cavities of Na<sub>3</sub>SbS<sub>4</sub>. The energy-dispersive X-ray (EDX) mapping in Figure 3f highlights the distribution of polymer electrolyte (C, O, and Cl elements) and the Na<sub>3</sub>SbS<sub>4</sub> electrolyte (Na, Sb, and S elements) in the trilayer structure.

Figure 3g shows the Arrhenius plot of conductivity ( $\sigma$ ) versus  $1000/T$  for three electrolytes employing EIS characterization using ionic blocking contact. In the temperature range of 20–80 °C, the Arrhenius plot of ionic conductivity of CPEO/Na<sub>3</sub>SbS<sub>4</sub>/CPEO shows a two-region behavior with an abrupt change at 56 °C, which is the melting point of PEO (Figure S5). Above 56 °C PEO transforms from semicrystal-

line to amorphous phase with higher Na<sup>+</sup> mobility. The similar conductivity trend observed between CPEO and trilayer electrolyte suggests the ionic conduction of the trilayer electrolyte is limited by the conductivity of CPEO. A Na–Na symmetric cell was assembled using the CPEO/Na<sub>3</sub>SbS<sub>4</sub>/CPEO trilayer electrolyte (Figure 4a). After resting the assembled cell at 60 °C for 1 h, the symmetric cell was charged and discharged under a current density of 0.1 mA cm<sup>-2</sup> for 0.5 h of Na plating and stripping, respectively. Figure 4a shows that after 800 h of cycling, the electrolyte shows no color change, in contrast to the blackening when CPEO interlayer is absent (Figure 1a). As shown in Figure 4c, the voltage polarization increased from 0.1 to 0.2 V in the beginning 30 cycles which was attributed to the SEI formation between the PEO and Na metal anode,<sup>23</sup> and then became stabilized at about 0.2 V and lasted for 800 h without an appreciable increase. The Nyquist plots for the EIS measurements (Figure 4b) are fitted based on the equivalent circuit shown in the inset, and the fitting parameters are summarized in Table S2. The initial value of  $R_b$  is approximately the same

during the cycling (from 95.2 to 98.8  $\Omega$ ). The interfacial resistance comprises of the contribution from the  $\text{Na}_3\text{SbS}_4/\text{CPEO}$  interface ( $R_1$ ) and the  $\text{CPEO}/\text{Na}$  interface ( $R_2$ ). The sum of  $R_1$  and  $R_2$  arises from 799.3 to 1,422.4  $\Omega$ , much lower than in the case when CPEO is absent (Figure 1c, 318.2 to 6475.0  $\Omega$ ). The  $R_{ct}$  also showed little increase (from 219.7 to 293.4  $\Omega$ ).

The XRD and XPS results further support the stability of the  $\text{Na}/\text{CPEO}/\text{Na}_3\text{SbS}_4$  interface. After 800 cycles, the symmetric cell was disassembled inside an argon-filled glovebox and the CPEO layer was carefully peeled off to expose the  $\text{Na}_3\text{SbS}_4$  surface for characterization. Figure S6 shows that the XRD pattern of the cycled sample was the same as that of pristine  $\text{Na}_3\text{SbS}_4$  powder. No  $\text{Na}_2\text{S}$  peaks were identified. The S 2p XPS spectra can be fitted into two spin-orbit doublets, corresponding to  $\text{Sb}=\text{S}$  and  $\text{Sb}-\text{S}-\text{Na}$  bond (Figure 4d). The signal of  $\text{Na}-\text{S}$  bond was not detected. Similarly, the Sb 3d spectra of pristine and cycled sample both indicate  $\text{Sb}^{5+}$  only (Figure 4d). These results indicate that the  $\text{Na}/\text{CPEO}/\text{Na}_3\text{SbS}_4$  interface is stable.

Previous efforts using polymer interlayer for Na metal protection was demonstrated by Goodenough et al., who showed a polymer/NASICON/polymer trilayer electrolyte with stable Na cycling for 384 h at 65  $^\circ\text{C}$ .<sup>24</sup> Because NASICON is chemically stable with Na metal, the purpose of polymer interlayer is to improve Na wettability toward NASICON and provide a uniform Na-ion flux at the interface. In this work, the polymer interlayer is designed for sulfide-based solid-state electrolytes to shut off the decomposition pathway. The stabilized metal/electrolyte interface leads to the stable cycling of a  $\text{Na}-\text{Na}$  symmetric cell for 800 h under 0.1  $\text{mA cm}^{-2}$ . Despite the apparent benefits of the CPEO interlayer on stabilizing the interface, the electrochemical stability is achieved at the expense of a larger voltage polarization (Figure 4c) because of lower conductivity of the CPEO layer. Although the reported  $\text{Na}-\text{Na}$  symmetric cell tests summarized in Table S1 are performed at room temperature, the symmetric cell built with polymer interlayer is cycled at an elevated temperature, as the low conductivity of the polymer layer at room-temperature leads to a large cell ASR (Figure S7). Because the resistance of the polymer layer is dependent on the thickness of the film and its intrinsic conductivity, strategies such as preparing ultrathin polymer layer via spin coating<sup>25</sup> or increasing the bulk conductivity of the polymer by adding an inorganic filler are beneficial for reducing the polarization at higher current densities.<sup>26</sup> Very recently, Ceder et al. reported that the interfacial stability between  $\text{Na}_3\text{SbS}_4$  and Na can be enhanced via a hydration phase  $\text{Na}_3\text{SbS}_4 \cdot 8\text{H}_2\text{O}$ , whose decomposition products ( $\text{NaH}$  and  $\text{Na}_2\text{O}$  etc.) form a passivation layer and suppress the  $\text{Na}_3\text{SbS}_4$  decomposition.<sup>27</sup> Their work offers a new design strategy using hydrates to stabilize of the metal-electrolyte interface.

In summary, we demonstrate that  $\text{Na}_3\text{SbS}_4$  is unstable with Na metal and will decompose into  $\text{Na}_2\text{S}$  and Sb during electrochemical cycling, as confirmed by both thermodynamic calculation and experimental measurements. By using a cellulose-poly(ethylene oxide) interlayer that only conducts ions but not electrons, the interface can become stable due to the absence of electronic pathway for the electrolyte decomposition reaction, resulting in a stable Na stripping/plating for 800 h at 60  $^\circ\text{C}$ . This simple method can also be

extended to improve the interfacial stability of other sulfide-based electrolytes with metal electrodes.

## ■ ASSOCIATED CONTENT

### Supporting Information

The Supporting Information is available free of charge on the ACS Publications website at DOI: 10.1021/acsami.8b19984.

Materials synthesis, device fabrication, EIS fitting parameters, XRD patterns, DSC results, Raman spectrum, and calculated phase diagram and voltage window (PDF)

## ■ AUTHOR INFORMATION

### Corresponding Author

\*Email: yyao4@uh.edu.

### ORCID

Fang Hao: 0000-0002-7701-6874

Hui Dong: 0000-0003-0169-0069

Lars C. Grabow: 0000-0002-7766-8856

Yan Yao: 0000-0002-8785-5030

### Author Contributions

P.H. and Y.Z. contributed equally to this work. P.H. and Y.Y. conceived the concept and designed the experiments. P.H., Y.Z., X.C., and F.H. conducted the synthesis, most of the characterizations, and the electrochemical measurement. H.D. contributed to XPS and EDS measurements. F.G. and R.Y. contributed to synchrotron measurements. K.K.R. and L.C.G. contributed the theoretical stability calculations. All authors discussed the results and commented on the final manuscript.

### Notes

The authors declare no competing financial interest.

## ■ ACKNOWLEDGMENTS

We thank the Solid Sodium team led by Prof. Steve Martin for technical discussion and thank Dr. Cheng-Jun Sun for the assistance in XANES measurement. Y.Y. acknowledges the funding support from the Advanced Research Projects Agency-Energy (award number: DE-AR0000654) and SeFAC seed funding from the Center for Advanced Computing and Data Systems (CACDS) at the University of Houston. K.K.R. acknowledges the NASA Space Technology Research Fellowship (80NSSC17K0148). This research used resources of the Advanced Photon Source, a U.S. Department of Energy (DOE) Office of Science User Facility operated for the DOE Office of Science by Argonne National Laboratory under Contract DE-AC02-06CH11357.

## ■ REFERENCES

- (1) Yabuuchi, N.; Kubota, K.; Dahbi, M.; Komaba, S. Research Development on Sodium-Ion Batteries. *Chem. Rev.* **2014**, *114* (23), 11636–11682.
- (2) Zhao, C.; Liu, L.; Qi, X.; Lu, Y.; Wu, F.; Zhao, J.; Yu, Y.; Hu, Y.-S.; Chen, L. Solid-State Sodium Batteries. *Adv. Energy Mater.* **2018**, *8* (17), 1703012.
- (3) Wang, H.; Wang, C.; Matios, E.; Li, W. Facile Stabilization of the Sodium Metal Anode with Additives: Unexpected Key Role of Sodium Polysulfide and Adverse Effect of Sodium Nitrate. *Angew. Chem., Int. Ed.* **2018**, *57* (26), 7734–7737.
- (4) Goodenough, J. B.; Hong, H. Y. P.; Kafalas, J. A. Fast Na-Ion Transport in Skeleton Structures. *Mater. Res. Bull.* **1976**, *11* (2), 203–220.

- (5) Hayashi, A.; Noi, K.; Sakuda, A.; Tatsumisago, M. Superionic Glass-Ceramic Electrolytes for Room-Temperature Rechargeable Sodium Batteries. *Nat. Commun.* **2012**, *3*, 856.
- (6) Kim, J.-J.; Yoon, K.; Park, I.; Kang, K. Progress in the Development of Sodium-Ion Solid Electrolytes. *Small Methods* **2017**, *1* (10), 1700219.
- (7) Hao, F.; Han, F.; Liang, Y.; Wang, C.; Yao, Y. Architectural Design and Fabrication Approaches for Solid-State Batteries. *MRS Bull.* **2018**, *43* (10), 775–781.
- (8) Zhu, Y.; He, X.; Mo, Y. Origin of Outstanding Stability in the Lithium Solid Electrolyte Materials: Insights from Thermodynamic Analyses Based on First-Principles Calculations. *ACS Appl. Mater. Interfaces* **2015**, *7* (42), 23685–23693.
- (9) Tang, H.; Deng, Z.; Lin, Z.; Wang, Z.; Chu, I.-H.; Chen, C.; Zhu, Z.; Zheng, C.; Ong, S. P. Probing Solid–Solid Interfacial Reactions in All-Solid-State Sodium-Ion Batteries with First-Principles Calculations. *Chem. Mater.* **2018**, *30* (1), 163–173.
- (10) Wenzel, S.; Weber, D. A.; Leichtweiss, T.; Busche, M. R.; Sann, J.; Janek, J. Interphase Formation and Degradation of Charge Transfer Kinetics between a Lithium Metal Anode and Highly Crystalline  $\text{Li}_7\text{P}_3\text{S}_{11}$  Solid Electrolyte. *Solid State Ionics* **2016**, *286*, 24–33.
- (11) Tian, Y.; Shi, T.; Richards, W. D.; Li, J.; Kim, J. C.; Bo, S.-H.; Ceder, G. Compatibility Issues between Electrodes and Electrolytes in Solid-State Batteries. *Energy Environ. Sci.* **2017**, *10* (5), 1150–1166.
- (12) Wenzel, S.; Leichtweiss, T.; Weber, D. A.; Sann, J.; Zeier, W. G.; Janek, J. Interfacial Reactivity Benchmarking of the Sodium Ion Conductors  $\text{Na}_3\text{PS}_4$  and Sodium  $\beta$ -Alumina for Protected Sodium Metal Anodes and Sodium All-Solid-State Batteries. *ACS Appl. Mater. Interfaces* **2016**, *8* (41), 28216–28224.
- (13) Chi, X.; Liang, Y.; Hao, F.; Zhang, Y.; Whiteley, J.; Dong, H.; Hu, P.; Lee, S.; Yao, Y. Tailored Organic Electrode Material Compatible with Sulfide Electrolyte for Stable All-Solid-State Sodium Batteries. *Angew. Chem., Int. Ed.* **2018**, *57* (10), 2630–2634.
- (14) Wan, H.; Mwirerwa, J. P.; Qi, X.; Xu, X.; Li, H.; Zhang, Q.; Cai, L.; Hu, Y.-S.; Yao, X. Nanoscaled  $\text{Na}_3\text{PS}_4$  Solid Electrolyte for All-Solid-State  $\text{FeS}_2/\text{Na}$  Batteries with Ultrahigh Initial Coulombic Efficiency of 95% and Excellent Cyclic Performances. *ACS Appl. Mater. Interfaces* **2018**, *10* (15), 12300–12304.
- (15) Wu, E. A.; Kompella, C. S.; Zhu, Z.; Lee, J. Z.; Lee, S. C.; Chu, I.-H.; Nguyen, H.; Ong, S. P.; Banerjee, A.; Meng, Y. S. New Insights into the Interphase between the Na Metal Anode and Sulfide Solid-State Electrolytes: A Joint Experimental and Computational Study. *ACS Appl. Mater. Interfaces* **2018**, *10* (12), 10076–10086.
- (16) Zhang, L.; Zhang, D.; Yang, K.; Yan, X.; Wang, L.; Mi, J.; Xu, B.; Li, Y. Vacancy-Contained Tetragonal  $\text{Na}_3\text{SbS}_4$  Superionic Conductor. *Adv. Sci.* **2016**, *3* (10), 1600089.
- (17) Wang, H.; Chen, Y.; Hood, Z. D.; Sahu, G.; Pandian, A. S.; Keum, J. K.; An, K.; Liang, C. An Air-Stable  $\text{Na}_3\text{SbS}_4$  Superionic Conductor Prepared by a Rapid and Economic Synthetic Procedure. *Angew. Chem.* **2016**, *128* (30), 8693–8697.
- (18) Banerjee, A.; Park, K. H.; Heo, J. W.; Nam, Y. J.; Moon, C. K.; Oh, S. M.; Hong, S.-T.; Jung, Y. S.  $\text{Na}_3\text{SbS}_4$ : A Solution Processable Sodium Superionic Conductor for All-Solid-State Sodium-Ion Batteries. *Angew. Chem.* **2016**, *128* (33), 9786–9790.
- (19) Dik, J.; Janssens, K.; Van Der Snickt, G.; van der Loeff, L.; Rickers, K.; Cotte, M. Visualization of a Lost Painting by Vincent van Gogh Using Synchrotron Radiation Based X-ray Fluorescence Elemental Mapping. *Anal. Chem.* **2008**, *80* (16), 6436–6442.
- (20) Ong, S. P.; Wang, L.; Kang, B.; Ceder, G. Li–Fe–P–O<sub>2</sub> Phase Diagram from First Principles Calculations. *Chem. Mater.* **2008**, *20* (5), 1798–1807.
- (21) Hautier, G.; Jain, A.; Chen, H.; Moore, C.; Ong, S. P.; Ceder, G. Novel Mixed Polyanions Lithium-ion Battery Cathode Materials Predicted by High-Throughput *ab initio* Computations. *J. Mater. Chem.* **2011**, *21* (43), 17147–17153.
- (22) Jain, A.; Ong, S. P.; Hautier, G.; Chen, W.; Richards, W. D.; Dacek, S.; Cholia, S.; Gunter, D.; Skinner, D.; Ceder, G.; Persson, K. A. Commentary: The Materials Project: A materials Genome Approach to Accelerating Materials Innovation. *APL Mater.* **2013**, *1* (1), 011002.
- (23) Qi, X.; Ma, Q.; Liu, L.; Hu, Y.-S.; Li, H.; Zhou, Z.; Huang, X.; Chen, L. Sodium Bis(fluorosulfonyl)imide/Poly(ethylene oxide) Polymer Electrolytes for Sodium-Ion Batteries. *ChemElectroChem* **2016**, *3* (11), 1741–1745.
- (24) Zhou, W.; Li, Y.; Xin, S.; Goodenough, J. B. Rechargeable Sodium All-Solid-State Battery. *ACS Cent. Sci.* **2017**, *3* (1), 52–57.
- (25) Park, C.-H.; Park, M.; Yoo, S.-I.; Joo, S.-K. A Spin-Coated Solid Polymer Electrolyte for All-Solid-State Rechargeable Thin-Film Lithium Polymer Batteries. *J. Power Sources* **2006**, *158* (2), 1442–1446.
- (26) Lin, D.; Liu, W.; Liu, Y.; Lee, H. R.; Hsu, P.-C.; Liu, K.; Cui, Y. High Ionic Conductivity of Composite Solid Polymer Electrolyte via In Situ Synthesis of Monodispersed  $\text{SiO}_2$  Nanospheres in Poly(ethylene oxide). *Nano Lett.* **2016**, *16* (1), 459–465.
- (27) Tian, Y.; Sun, Y.; Hannah, D. C.; Xiao, Y.; Liu, H.; Chapman, K. W.; Bo, S.-H.; Ceder, G. Reactivity-Guided Interface Design in Na Metal Solid-State Batteries. *Joule* **2019**, *3*, 1–14.